Nonclassical cutoff fluctuations in squeezed-light-driven high-harmonic generation

Tsendsuren Khurelbaatar [1,2,*] R. T. Sang [1,2,3] and Igor V. Litvinyuk [1,2]

[1]*Queensland Quantum and Advanced Technologies Research Institute, Griffith University, Brisbane, Queensland 4111, Australia*

[2]*School of Environment and Science, Griffith University, Brisbane, Queensland 4111, Australia*

[3]*Office of the Pro Vice-Chancellor (Research, Development and Commercialisation), University of Southern Queensland, Springfield 4300, Australia*

(Received 20 May 2026; accepted 6 October 2026; published 30 October 2026)

In the conventional description of strong-field high-harmonic generation (HHG), the atom is treated quantum mechanically while the driving laser is represented by a classical field. Quantum fluctuations of the driver can become relevant in nanoscale interaction geometries, where tight spatial confinement can raise the vacuum-field amplitude to $\sim 10^{-2}$ of the mean driving-field amplitude. In this regime, fluctuations of a squeezed driver can imprint its quadrature statistics on HHG observables. To model this interaction, we sample the positive Wigner function of the driving field and solve the time-dependent Schrödinger equation for each sampled field realization. Within a single-mode Gaussian framework, we show that amplitude squeezing suppresses the shot-to-shot variance of the HHG cutoff below the coherent-state standard quantum limit (SQL) at the same mean field. To leading order in the vacuum-to-driver field ratio, the normalized variance follows e^{-2r}, where r is the squeezing parameter, independently of the absolute vacuum-field amplitude. At stronger squeezing, quadratic coupling of the antisqueezed quadrature to the field modulus competes with this suppression, yielding a variance minimum near $r_{\mathrm{opt}} \approx 1.55$ for the parameters studied. A sub-SQL cutoff variance thus indicates subvacuum noise in the quadrature probed by the cutoff, suggesting that shot-resolved HHG cutoff measurements could witness driving-field nonclassicality.

DOI: 10.1103/ffdj-mz2y

I. INTRODUCTION

High-harmonic generation (HHG) is central to attosecond science and is a strongly nonperturbative process whose essential features are captured by the semiclassical three-step model [1,2]. In the conventional treatment of this process, the driving laser is assumed to be a deterministic classical field, rendering photon statistics operationally irrelevant. This approximation is well justified in free-space focusing geometries, where the large quantization volume strongly suppresses the vacuum-field amplitude, making quantum fluctuations negligible relative to the amplitude of the driving field. Built upon this deterministic-field foundation, semiclassical strong-field theory has successfully described isolated attosecond-pulse generation [3,4], nonsequential double ionization [5,6], and a broad range of nonperturbative laser-matter phenomena.

Recent developments in quantum light sources, however, are beginning to challenge this established paradigm. Nonclassical fields such as bright squeezed vacuum [7–9] are now being used to drive strong-field processes, establishing strong-field quantum optics as a rapidly evolving experimental frontier [10–13]. These experimental advances have stimulated a growing theoretical effort to determine how nonclassical driving fields reshape strong-field observables. The photon statistics of the driver have been shown to directly affect the strong-field electron dynamics, introducing a degree of freedom absent from the conventional deterministic-field description [14]. In HHG, quantum light has been predicted to enable harmonic emission in geometries that remain forbidden for classical drivers, and to provide control over the quantum paths, polarization, and temporal structure of the emitted radiation [15–20]. The statistical properties of the driver can also be transferred to the emitted harmonics, generating nonclassical radiation with features such as squeezing [21,22]. In strong-field ionization, nonclassical driving statistics likewise modify ionization yields and photoelectron spectra [23]. Of particular relevance to the present work, phase-space treatments of both HHG and above-threshold ionization have shown that broad field-amplitude distributions increase the contribution of rare high-intensity realizations, thereby extending spectral plateaus and shifting their cutoff positions [15,24,25]. These studies demonstrate that strong-field observables are sensitive to the statistical properties of the driving field.

Here, we address the complementary question of whether HHG can serve as a quantum transducer by mapping quantum fluctuations of the incident driving field onto experimentally accessible observables. We show that the HHG cutoff variance

*Contact author: t.khurelbaatar@griffith.edu.au

Published by the American Physical Society under the terms of the Creative Commons Attribution 4.0 International license. Further distribution of this work must maintain attribution to the author(s) and the published article's title, journal citation, and DOI.

provides an operational probe of the amplitude-quadrature noise of the driving field, including its suppression below the coherent-state reference level. Realizing this transduction requires two conditions: First, the vacuum-field amplitude must be sufficiently large for quantum fluctuations of the driver to produce measurable variations in the HHG cutoff. This requirement favors nanoscale interaction geometries, including nanoplasmonic hot spots, metallic nanotips, semiconductor nanostructures, and dielectric metasurfaces [26–30], where strong spatial confinement reduces the effective mode volume. The resulting enhancement of the vacuum field can increase the relative field fluctuations to the order of 10^{-2} of the mean driving-field amplitude for typical strong-field intensities ($\sim 10^{14}$ W/cm^2), as discussed in Sec. II B. Second, these fluctuations must be controllable rather than isotropic. Squeezed light provides this control by redistributing the quadrature noise anisotropically, reducing it in one quadrature while enhancing it in the conjugate quadrature. Because the HHG cutoff responds differently to conjugate quadratures, it maps this quadrature-dependent noise onto experimentally accessible shot-to-shot cutoff variations.

To model this transduction, we sample the positive Wigner function of the driving field, producing a stochastic ensemble of field amplitudes that reproduces its quadrature statistics [31]. Each sampled field realization then serves as a prescribed classical driving field in an independent time-dependent Schrödinger equation (TDSE) calculation, mapping the quantum field statistics onto the corresponding distribution of single-shot HHG cutoffs. Within this framework, we obtain three main results. First, amplitude squeezing suppresses the HHG cutoff variance below the coherent-state standard quantum limit (SQL): The normalized cutoff-variance ratio $\mathcal{R} \equiv \Delta H^2/\Delta H^2_{\mathrm{SQL}}$, in which $\Delta H^2_{\mathrm{SQL}}$ is defined operationally as the cutoff variance obtained with a coherent-state driver at the same mean field and under otherwise identical experimental conditions, obeys the leading-order scaling

$$\mathcal{R} \simeq e^{-2r},$$

independent of the absolute vacuum-field amplitude for moderate amplitude squeezing. Second, the cutoff variance varies with the squeezing angle θ, mapping the orientation of the Wigner covariance ellipse onto the HHG response. Third, the enhanced conjugate-quadrature variance introduces competing noise channels, dominated by the quadratic coupling of the antisqueezed quadrature to the field modulus, which produce a variance minimum near $r_{\mathrm{opt}} \approx 1.55$. The cutoff-variance ratio therefore functions both as a self-normalized witness of driving-field nonclassicality and as a quantum transducer of conjugate-quadrature fluctuations into an experimentally accessible strong-field observable.

II. THEORETICAL FRAMEWORK

A. Squeezed coherent states

To capture the interplay between quantum statistics and strong-field dynamics, we employ squeezed coherent states (SCS), also referred to as displaced squeezed states: canonical nonclassical Gaussian states in which the quantum noise of one field quadrature is reduced below the vacuum level while that of the conjugate quadrature is correspondingly increased, redistributing rather than removing the Heisenberg-mandated uncertainty. In phase space, squeezing stretches the isotropic circular profile of a coherent state into an area-preserving ellipse, as illustrated in Figs. 1(a)–1(c).

The driving field is the SCS obtained by displacing the squeezed vacuum,

$$|\alpha, \xi\rangle = \hat{D}(\alpha)\,\hat{S}(\xi)|0\rangle, \tag{1}$$

defined by a complex displacement $\alpha = |\alpha|e^{i\phi}$ and a squeezing parameter $\xi = re^{i2\theta}$, where $r \geqslant 0$ denotes the squeezing magnitude and θ the orientation of the squeezed quadrature in phase space. The displacement, $\hat{D}(\alpha)$, is applied after the squeezing operator, $\hat{S}(\xi)$, so that α specifies the mean coherent amplitude and optical phase; we set $\phi = 0$ without loss of generality, so that the mean field lies along X. In this convention, $\theta = 0$ corresponds to amplitude squeezing (AS), which suppresses fluctuations of the in-phase quadrature X below the vacuum level, whereas $\theta = \pi/2$ corresponds to phase squeezing (PS), suppressing fluctuations of the orthogonal quadrature P. We adopt this correspondence as a fixed convention: Wherever a double sign ($\mp$ or $\pm$) appears in the following, the upper sign refers to AS ($\theta = 0$) and the lower sign to PS ($\theta = \pi/2$), with $r \geqslant 0$ in both cases.

For states aligned with the principal quadratures, these squeezed states saturate the Heisenberg uncertainty relation,

$$\sigma_X \sigma_P = \tfrac{1}{2}, \tag{2}$$

where σ_X and σ_P denote the standard deviations of the dimensionless quadratures.

Along these principal axes, the variances scale exponentially with r,

$$\sigma_X^2(r) = \tfrac{1}{2}e^{\mp 2r}, \quad \sigma_P^2(r) = \tfrac{1}{2}e^{\pm 2r}. \tag{3}$$

Atomic units ($\hbar = m_e = e = a_0 = 1$) are used throughout unless otherwise stated.

B. Wigner phase-space mapping

We incorporate the quantum fluctuations of the driving field by sampling its Wigner phase-space distribution. For an SCS, the Wigner function is a positive Gaussian and can therefore be sampled directly as an ensemble of quadrature pairs (X_i, P_i) [31–33]. Each pair defines a deterministic time-dependent field used in an independent TDSE calculation, and the resulting observables are averaged over the ensemble. This procedure preserves the quadrature statistics of the prepared optical state while treating the driver as an effective single mode with a fixed pulse envelope: The sampled quadratures generate shot-to-shot variations in carrier amplitude and phase, whereas multimode correlations, atom-field entanglement, driver depletion, and dynamical backaction on the driver are excluded (see the Supplemental Material [34]).

The Wigner distribution is

$$W(\mathbf{q}) = \frac{1}{2\pi\sqrt{\det \Sigma}} \exp\left[-\frac{1}{2}(\mathbf{q}-\bar{\mathbf{q}})^T \Sigma^{-1}(\mathbf{q}-\bar{\mathbf{q}})\right], \tag{4}$$

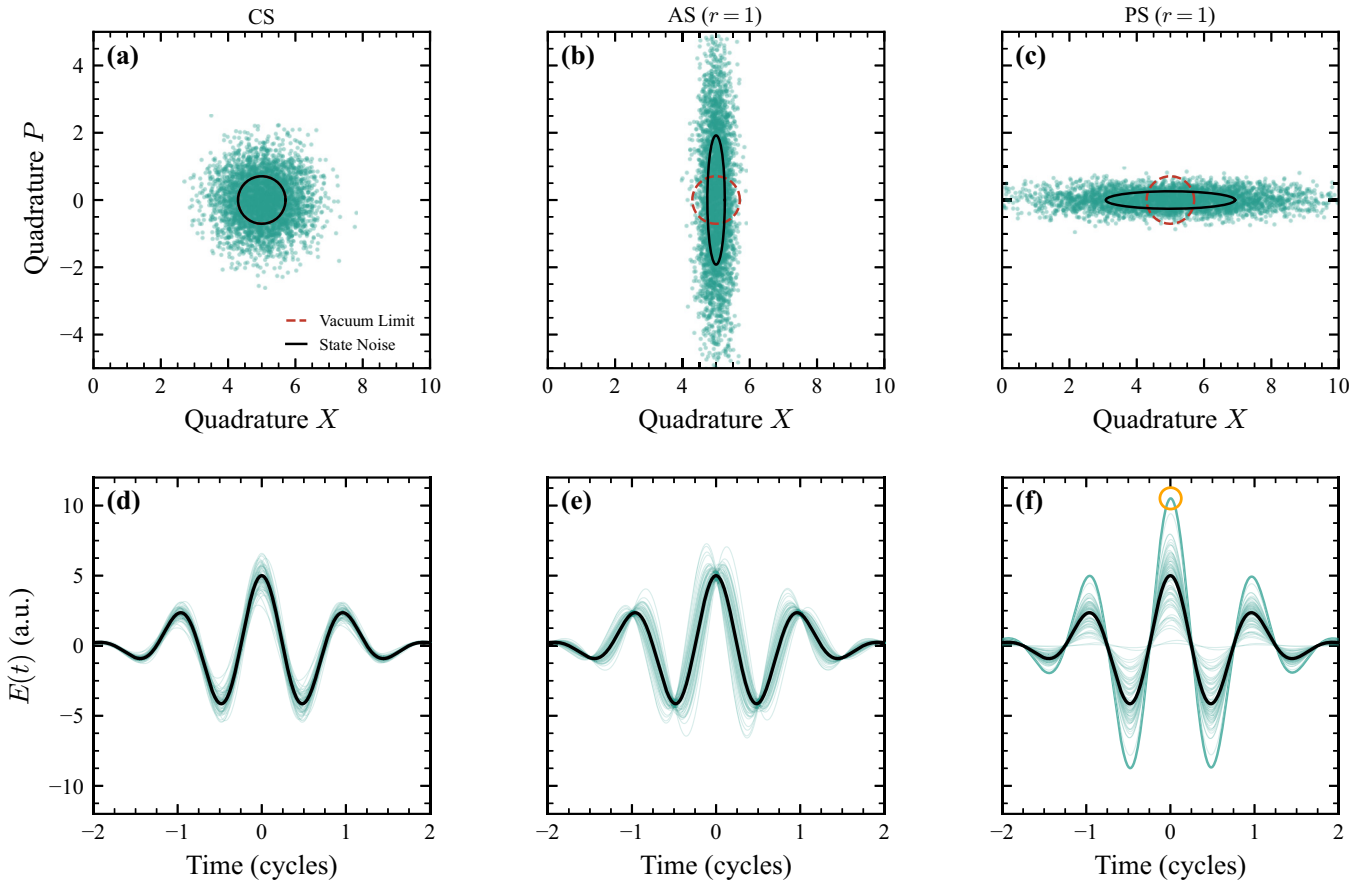


FIG. 1. Wigner phase-space representation and stochastic field realizations. Top row: Wigner distributions for (a) a coherent state (CS), (b) an amplitude-squeezed state (AS, $r = 1$), and (c) a phase-squeezed state (PS, $r = 1$). Teal points are sampled quadrature pairs (X_i, P_i); solid black ellipses show the 1σ contours; and dashed crimson circles indicate the coherent-state vacuum-noise contour. Bottom row: Corresponding time-domain field realizations for (d) coherent, (e) amplitude-squeezed, and (f) phase-squeezed driving. Thin teal lines show individual realizations, while the solid black line denotes the mean field. The highlighted high-amplitude realization in panel (f) illustrates the rare events that extend the HHG cutoff.

where $\mathbf{q} = (X, P)^T$, $\bar{\mathbf{q}} = (\sqrt{2}\,|\alpha|, 0)^T$, and

$$\Sigma(r, \theta) = R(\theta)\begin{pmatrix} \frac{1}{2}e^{-2r} & 0 \\ 0 & \frac{1}{2}e^{+2r} \end{pmatrix} R^T(\theta), \tag{5}$$

with $R(\theta)$ the phase-space rotation matrix. Because the driving field couples to the in-phase quadrature at the carrier maximum, the leading amplitude response is governed by the corresponding marginal variance, i.e., the leading diagonal element of Eq. (5). Its general angular form is required only for the angular sweep analyzed in Sec. III C and is given there [Eq. (21)].

Each sampled pair defines the field realization

$$E_i(t) = \mathcal{E}_{\text{vac}} \exp\left[-4 \ln 2 \left(\frac{\omega t}{2\pi N} \right)^2 \right] \times (X_i \cos \omega t + P_i \sin \omega t), \tag{6}$$

where ω is the carrier frequency, N is the field-envelope full width at half maximum (FWHM) in optical cycles, and

$$\mathcal{E}_{\text{vac}} = \sqrt{\frac{4\pi\omega}{V_{\text{eff}}}}. \tag{7}$$

Here, $\mathcal{E}_{\text{vac}}$ is the vacuum-field amplitude and V_{eff} the effective mode volume. With the present quadrature convention, the vacuum rms field is $\mathcal{E}_{\text{vac}}/\sqrt{2}$, and the mean peak field is $E_0 = \sqrt{2}\,\mathcal{E}_{\text{vac}}|\alpha|$. Representative realizations are shown in Figs. 1(d)–1(f). AS suppresses field-amplitude fluctuations [Fig. 1(e)], whereas PS broadens them and produces rare high-amplitude realizations [Fig. 1(f)] that extend the HHG cutoff.

C. Stochastic TDSE and the cutoff observable

We numerically solve the one-dimensional length-gauge TDSE for a soft-core argon model atom [38,39] driven by a linearly polarized $N = 2$ pulse (∼7.1 fs intensity FWHM) at $\lambda = 1500\,\text{nm}$ with a peak intensity $I_0 = 1 \times 10^{14}\,\text{W/cm}^2$. These parameters place the electron dynamics in the tunnel ionization regime, with Keldysh parameter $\gamma \simeq 0.6$ [40]. For each realization, the electric field $E_i(t)$ is sampled according to Eq. (6). Nanoscale spatial confinement is parametrized in the model by the effective mode volume V_{eff}, which determines the vacuum-field amplitude $\mathcal{E}_{\text{vac}}$. We consider a representative strong-confinement regime with $\mathcal{E}_{\text{vac}}/E_0 \sim 10^{-2}$; the corresponding mode-volume estimate, numerical

details, and convergence tests are provided in the Supplemental Material [34].

The HHG spectrum is calculated from the Fourier transform of the Ehrenfest dipole acceleration,

$$a_i(t) = \left\langle -\frac{\partial V}{\partial x} - E_i(t) \right\rangle, \tag{8}$$

following the standard approach of Refs. [41,42]. The resulting spectral intensity is

$$S_i(\Omega) = \left| \int_{-\infty}^{\infty} a_i(t)\, g(t)\, e^{-i\Omega t}\, \mathrm{d}t \right|^2, \tag{9}$$

where Ω is the emitted angular frequency, i labels the realization, and $g(t)$ is a Blackman window. From these spectra, we extract the cutoff position H, expressed in harmonic order (H.O.) as $H = E_{\mathrm{cutoff}}/\hbar\omega$, and its shot-to-shot variance $\Delta H^2 = \langle H^2 \rangle - \langle H \rangle^2$. For a given spectrum, H is defined as the spectral position at which the smoothed $\log_{10} S(\Omega)$ curve falls a predetermined number of decades below its characteristic plateau value (see the Supplemental Material [34]).

III. RESULTS

A. Ionization and statistical filtering

In the tunnel ionization regime ($\gamma < 1$) [40], the instantaneous ionization rate is highly nonlinear and is well described by the Ammosov-Delone-Krainov (ADK) formula [43]:

$$\Gamma(E) \sim A(E) \exp\left(-\frac{B}{|E|}\right), \tag{10}$$

where $B = \frac{2}{3}(2I_p)^{3/2}$ and $A(E)$ is a weakly field-dependent prefactor. The ensemble-averaged rate is obtained by averaging this rate over the field distribution:

$$\langle \Gamma \rangle = \int_{-\infty}^{\infty} \mathrm{d}E\; Q(E)\Gamma(E), \tag{11}$$

where $Q(E)$ represents the marginal field distribution at the carrier maximum.

The steep exponential structure of Eq. (10) effectively acts as a statistical filter. Rare, high-amplitude field realizations [e.g., see Fig. 1(f)] are weighted exponentially more strongly than fluctuations occurring near the mean field, as visualized in Fig. 2(a). Neglecting derivatives of the weakly varying prefactor $A(E)$, we expand the dominant tunneling exponent about E_0,

$$\ln \Gamma(E) = \ln \Gamma(E_0) + \frac{B}{E_0^2}\delta E - \frac{B}{E_0^3}\delta E^2 + \mathcal{O}(\delta E^3), \tag{12}$$

and, applying a cumulant expansion tailored to the Gaussian field distribution, obtain the leading correction to the ensemble-averaged rate:

$$\ln \frac{\langle \Gamma \rangle}{\Gamma(E_0)} \simeq \mathcal{E}_{\mathrm{vac}}^2 \sigma_X^2(r) \left(\frac{B^2}{2E_0^4} - \frac{B}{E_0^3} \right). \tag{13}$$

The bracketed coefficient captures two competing effects: a positive enhancement arising from the squared linear term in Eq. (12) and a partial cancellation from the negative quadratic correction. For the physical parameters considered here, the first term dominates, resulting in a net rate enhancement whenever the amplitude distribution is broadened. If we define the dimensional vacuum-field variance $\sigma_{\mathrm{vac}}^2 = \mathcal{E}_{\mathrm{vac}}^2/2$ and the dimensionless ionization-sensitivity parameter

$$\zeta = \sigma_{\mathrm{vac}}^2 \left(\frac{B^2}{2E_0^4} - \frac{B}{E_0^3} \right), \tag{14}$$

the ensemble-averaged rate, normalized to the coherent-state ensemble-averaged rate (Γ_{coh}), simplifies to

$$\frac{\langle \Gamma \rangle}{\Gamma_{\mathrm{coh}}} \simeq \exp[\zeta(e^{\mp 2r} - 1)]. \tag{15}$$

Since $\zeta > 0$ for the parameters considered here, the rate is enhanced whenever the sampled amplitude variance exceeds

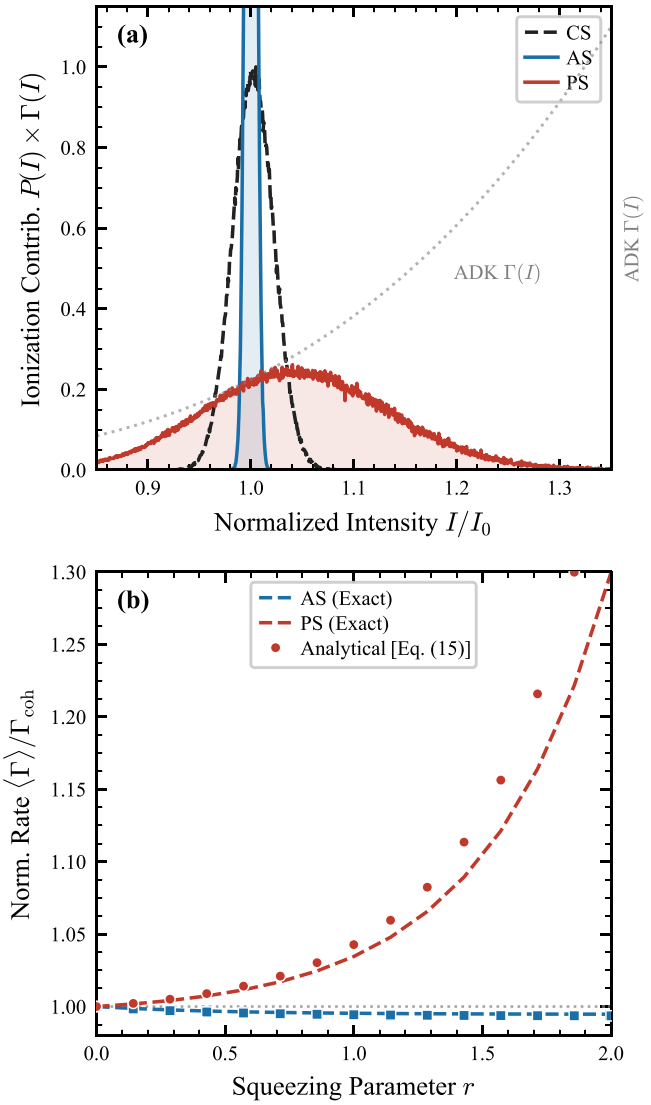


FIG. 2. Statistical filtering of tunnel ionization. (a) Ionization contribution $P(I)\Gamma(I)$ vs normalized intensity I/I_0 for CS (black dashed), AS (blue), and PS (red shaded). The bare ADK rate $\Gamma(I)$ (gray dotted, right axis) illustrates exponential weighting toward rare high-intensity realizations. (b) Normalized ensemble-averaged ionization rate $\langle \Gamma \rangle / \Gamma_{\mathrm{coh}}$ vs r, comparing numerical evaluation of Eq. (11) for AS (blue dashed) and PS (red dashed) with the analytical approximation of Eq. (15) (filled symbols).

the vacuum level: PS gives an enhancement, whereas AS gives a slight suppression.

Figure 2(b) demonstrates that this statistical enhancement is sensitive to the specific quadrature variance. PS states exhibit a monotonic rate enhancement due to their broadened amplitude statistics. Conversely, AS states produce little modification; their suppressed amplitude fluctuations are transferred into the phase quadrature, which does not couple at leading order to the tunneling exponent in the carrier-maximum amplitude expansion used here. We emphasize that this enhancement is a statistical consequence, not an exclusively quantum one: Any classical field possessing an identical marginal amplitude distribution would generate the same rate response. The role of the squeezed state here is to provide an experimentally tunable, minimum-uncertainty redistribution of the quadrature fluctuations. Quantum signatures emerge when examining fluctuations of the HHG cutoff.

B. HHG cutoff extension

The statistical filtering of the ionization step fundamentally shapes the ensemble-averaged HHG spectrum. Figure 3(a) displays the ensemble-averaged HHG spectra computed at a fixed mean field E_0. Compared with the CS reference, the PS driver shifts the cutoff by several tens of harmonic orders, whereas the AS spectrum remains close to the CS reference. This cutoff extension is a direct ensemble-level consequence of the statistical filtering detailed in Sec. III A: A small subset of high-amplitude stochastic realizations contributes disproportionately to the ensemble, generating larger ponderomotive energies and pushing the ensemble cutoff beyond the mean-field prediction. The standard classical cutoff law provides an approximate description of each realization,

$$E_{\text{cutoff}} = I_p + 3.17U_p(E), \tag{16}$$

where I_p is the ionization potential and $U_p(E) = E^2/4\omega^2$ is the ponderomotive energy of an electron oscillating in a field of amplitude E and carrier frequency ω, evaluated at the field amplitude of that realization. The observed extension emerges upon statistical averaging over the ensemble.

The statistic we analyze quantitatively is the rate-weighted mean cutoff, defined as

$$E^{\Gamma}_{\text{cutoff}} \equiv I_p + 3.17\frac{\langle \Gamma(E)U_p(E)\rangle}{\langle \Gamma(E)\rangle}, \tag{17}$$

where each realization is weighted by its own tunneling rate. This rate-weighted mean differs from the cutoff of the ensemble-averaged spectrum in Fig. 3(a). By expanding $U_p(E)$ about E_0 and combining this expansion with the preceding expansion of the ADK rate, we obtain an analytical approximation for the rate-weighted mean cutoff:

$$E^{\Gamma}_{\text{cutoff}}(r) \simeq I_p + 3.17U_p(E_0)\left[1 + \epsilon^2(r)\left(1 + \frac{2B}{E_0}\right)\right], \tag{18}$$

which is valid in the small-fluctuation limit. Here, the small parameter ϵ is the rms amplitude fluctuation of the sampled quadrature relative to the mean driving field,

$$\epsilon(r) = \frac{\mathcal{E}_{\text{vac}}}{\sqrt{2}E_0}\, e^{\mp r}. \tag{19}$$

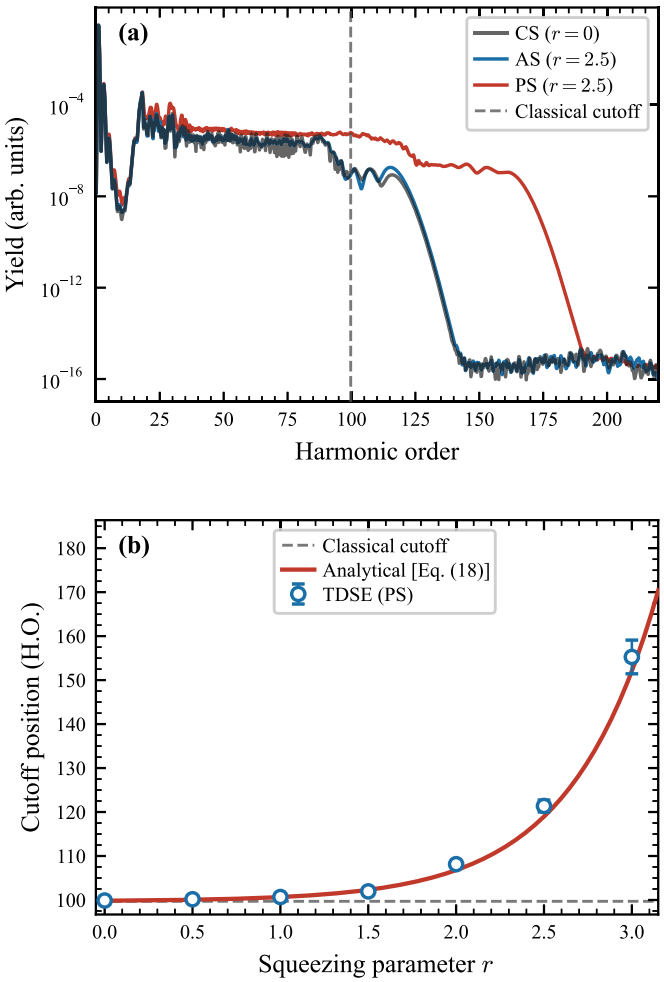


FIG. 3. HHG cutoff extension under squeezed-field driving. (a) Ensemble-averaged HHG spectra for a CS reference (black) and AS (blue) and PS (red) drivers with $r = 2.5$. The gray dashed line is the classical cutoff $[I_p + 3.17U_p(E_0)]/\hbar\omega = 99.7$ H.O. (b) Rate-weighted mean cutoff vs r on the phase-squeezed branch (open circles; $N_{\text{shots}} = 1000$ shot-resolved realizations per r), compared with Eq. (18) (red solid) and the classical cutoff (gray dashed). Error bars are the standard error of the weighted mean.

The validity of this expansion depends both on ϵ and on the sensitivity of the tunneling exponent to these fluctuations, which is characterized by $(B/E_0)\,\epsilon$, with $B/E_0 \simeq 15.6$. These conditions bound the two branches differently. Under PS, the sampled amplitude fluctuation grows as e^{+r}, so Eq. (18) holds only up to a maximum squeezing strength; under AS, it decreases as e^{-r}, so ϵ itself imposes no upper bound. The AS branch is instead limited by the antisqueezed P quadrature, which introduces corrections not controlled by ϵ [cf. the $C_{P^2}e^{+4r}$ channel of Eq. (24) and Fig. 4(d)]. Figure 3(b) compares Eq. (18) with the TDSE-extracted cutoffs on the PS branch. Agreement is good over the moderate-squeezing range $r \lesssim 1.5$; at larger r, the analytical curve departs from the TDSE result as higher-order terms neglected in the small-fluctuation expansion become non-negligible.

While the cutoff extension demonstrates sensitivity to the underlying field statistics, it does not intrinsically establish nonclassicality: An engineered classical stochastic field with

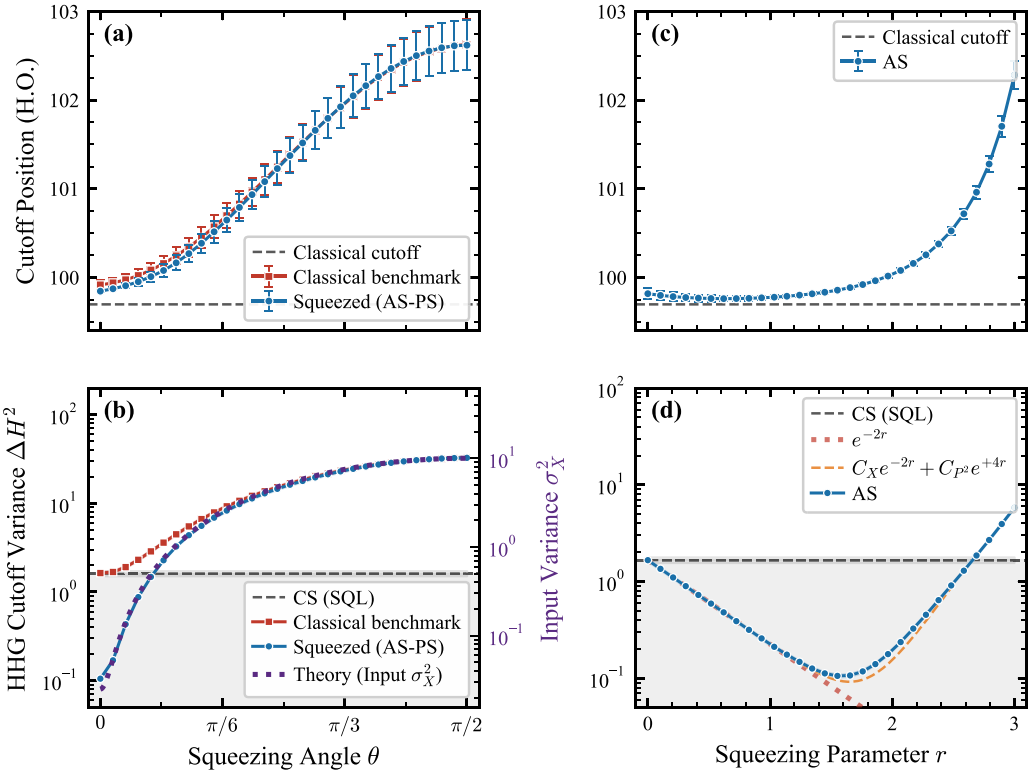


FIG. 4. Quadrature-resolved HHG cutoff statistics. (a) Rate-weighted cutoff position vs squeezing angle θ at a fixed $r = 1.5$ for the squeezed state (blue circles) and the classical $\mathcal{P} \geqslant 0$ benchmark (dark red squares). Error bars are the standard error of the weighted mean. (b) HHG cutoff variance ΔH^2 vs θ. The squeezed state (blue circles) falls below the coherent-state SQL at $\theta = 0$ and remains sub-SQL up to $\theta \simeq 12.6^\circ$; the classical benchmark (dark red squares) remains SQL-bounded for all θ. Shading marks the sub-SQL region. The right axis and purple dotted curve show the input quadrature variance $\sigma_X^2(\theta)$, referenced to the vacuum variance $1/2$, confirming that ΔH^2 tracks $\sigma_X^2(\theta)$ across the full angular sweep. (c) Rate-weighted cutoff position (blue circles) and (d) HHG cutoff variance ΔH^2 vs r under amplitude squeezing (AS). The leading-order e^{-2r} scaling [Eq. (23)] is shown by the red dotted curve. The two-channel model [Eq. (24)] is shown by the orange dashed curve. In panels (a) and (c), the gray dashed line shows the mean-field classical cutoff. Each data point is obtained from an ensemble of $N_{\text{shots}} = 1000$ shots.

matched amplitude statistics would reproduce an identical cutoff shift. To find a decisive distinction, we must look to the fluctuations of the HHG cutoff.

C. Quadrature-resolved cutoff statistics

To establish a classicality criterion, it is important to distinguish Wigner positivity from optical classicality. The SCS considered here have positive Gaussian Wigner functions, and Hudson's theorem identifies Gaussian states as the only pure states with non-negative Wigner functions [44]. This positivity, however, does not imply classicality. The Wigner representation is less restrictive than the Glauber-Sudarshan $\mathcal{P}$ representation: The Wigner function is obtained by Gaussian smoothing of the $\mathcal{P}$ distribution and can therefore remain positive even when no non-negative $\mathcal{P}$ distribution exists. A single-mode field is classical in the quantum-optical sense if it admits a non-negative Glauber-Sudarshan representation ($\mathcal{P} \geqslant 0$) [45,46]. Such a field is a statistical mixture of coherent states, and its quadrature covariance can therefore be written as

$$\Sigma = \tfrac{1}{2}\mathbb{I} + \Sigma_{\text{exc}}, \quad \Sigma_{\text{exc}} \succeq 0, \tag{20}$$

where $\frac{1}{2}\mathbb{I}$ is the vacuum contribution and Σ_{exc} represents classical excess fluctuations. Consequently, the variance along any rotated quadrature $X_\varphi = X\cos\varphi + P\sin\varphi$ satisfies $\sigma_{X_\varphi}^2 \geqslant 1/2$, irrespective of classical cross-correlations. A subvacuum quadrature variance therefore provides a sufficient witness of optical nonclassicality.

For the strong-field interaction considered here, the field amplitude at the carrier maximum is governed, to leading order, by the X quadrature. The sampled amplitude variance at squeezing angle θ is

$$\sigma_X^2(r,\theta) = \tfrac{1}{2}(e^{-2r}\cos^2\theta + e^{+2r}\sin^2\theta). \tag{21}$$

We therefore construct a Gaussian classical benchmark that retains the orientation and antisqueezed principal variance of the squeezed state while replacing its subvacuum principal variance by the vacuum limit,

$$\Sigma_{\text{cl}}(\theta) = R(\theta)\begin{pmatrix} 1/2 & 0 \\ 0 & \frac{1}{2}e^{+2r} \end{pmatrix} R^T(\theta). \tag{22}$$

Since $\Sigma_{\text{cl}} - \frac{1}{2}\mathbb{I} \succeq 0$, this covariance admits a non-negative Gaussian $\mathcal{P}$ representation and hence constitutes a classical reference with the same antisqueezed noise scale. Relative to the squeezed state, the benchmark's sampled amplitude

variance is increased only by $\frac{1}{2}(1-e^{-2r})\cos^2\theta$. This difference is largest for amplitude squeezing ($\theta = 0$), where the benchmark reaches the classical lower bound $\sigma^2_{X,\mathrm{cl}} = 1/2$. Any further suppression of the amplitude variance at this orientation therefore directly certifies nonclassicality.

Having established this classicality criterion and the corresponding Gaussian benchmark, we now compare its HHG response directly with that of the squeezed-state driver. The HHG cutoff position is closely reproduced by the classical benchmark. Figure 4(a) plots the rate-weighted mean HHG cutoff position versus θ at a fixed $r = 1.5$, consistent with Eq. (18). The normalized cutoff variance, however, distinguishes between the two regimes [Fig. 4(b)]. The classical benchmark remains SQL-bounded for all θ, whereas the squeezed state falls below the SQL, reaching a minimum at $\theta = 0$. Across the full angular sweep, ΔH^2 tracks $\sigma^2_X(\theta)$, yielding a quadrature-resolved mapping between the input quadrature covariance and the cutoff observable. This separates sensitivity to field statistics from certification of optical nonclassicality. The cutoff shift is governed by the marginal amplitude distribution and can therefore be reproduced by a classical stochastic field with the same distribution [Fig. 4(a)], whereas the cutoff fluctuations transduce the driving-field quadrature noise. Within the linear-response regime, where the tested and coherent-state drivers share the same cutoff response coefficient, a cutoff variance below the coherent-state SQL thus witnesses subvacuum noise in the sampled quadrature and is incompatible with any single-mode state admitting a non-negative Glauber-Sudarshan $\mathcal{P}$ representation: The nonclassical signature resides not in the cutoff extension, but in the covariance-sensitive cutoff fluctuations [Fig. 4(b)].

Figures 4(c) and 4(d) show the cutoff position and the variance ΔH^2 as functions of r under amplitude squeezing ($\theta = 0$). The cutoff variance initially decreases, reaches a minimum around $r_{\mathrm{opt}} \approx 1.55$, and then increases. To understand the initial suppression, we linearize the classical cutoff relationship [Eq. (16)] about E_0, obtaining $\delta H \simeq (\partial H/\partial E)|_{E_0}\delta E$. The response coefficient is identical for quantum and classical drivers evaluated at the same E_0. The resulting leading-order variance is $\Delta H^2 \simeq (\partial H/\partial E)^2\sigma^2_{\delta E}$, with $\sigma^2_{\delta E} = \mathcal{E}^2_{\mathrm{vac}}\sigma^2_X(r,\theta = 0)$ for AS. Normalizing this expression by the coherent-state variance at the same mean field cancels both the linear-response prefactor and the absolute vacuum-field amplitude:

$$\mathcal{R}(r) \equiv \frac{\Delta H^2(r)}{\Delta H^2_{\mathrm{SQL}}} \simeq \frac{\sigma^2_X(r,\theta=0)}{\sigma^2_{X,\mathrm{vac}}} = e^{-2r}. \tag{23}$$

At fixed r, Eq. (23) is the leading-order result in the vacuum-to-driver field ratio $\mathcal{E}_{\mathrm{vac}}/E_0$. This constitutes the central result of our work: The normalized cutoff variance provides a nonclassicality witness whose leading-order scaling is determined solely by the squeezing parameter and is independent of the absolute vacuum-field amplitude. This scaling is observed in the $r \lesssim 1.2$ region of Fig. 4(d).

The subsequent upturns in the cutoff position and variance are absent from the leading-order description: Both Eqs. (18) and (23) are controlled by the sampled amplitude variance $\sigma^2_X = \frac{1}{2}e^{-2r}$, which amplitude squeezing suppresses monotonically. These upturns arise from the quadratic coupling of the orthogonal quadrature to the field modulus. Geometrically, the conjugate quadrature is orthogonal to the mean displacement, so it cannot shift the peak driving amplitude at first order and enters through the field modulus $\sqrt{X^2+P^2}$. Its growing fluctuations therefore shift the mean cutoff and introduce an additional variance channel. With $\mathrm{Var}(\delta P^2) = 2\sigma^4_P$ for Gaussian fluctuations, this contribution to the variance scales as e^{+4r}. Retaining the leading amplitude contribution and this conjugate-quadrature correction gives

$$\Delta H^2(r) \simeq C_X\, e^{-2r} \;+\; C_{P^2}\, e^{+4r}. \tag{24}$$

The competition between these two channels produces the observed minimum in Fig. 4(d). Because the cutoff is quadratic in the field, the strong-field response cancels in the ratio of the two coefficients, which is fixed by the vacuum-to-driver field ratio alone, $\kappa \equiv C_{P^2}/C_X = \frac{1}{4}(\mathcal{E}_{\mathrm{vac}}/E_0)^2$. The minimum of Eq. (24) therefore occurs at

$$r_{\mathrm{opt}} = \frac{1}{6}\ln\!\left(\frac{1}{2\kappa}\right). \tag{25}$$

For the present parameters, this gives $r_{\mathrm{opt}} \simeq 1.65$, within ~6% of the TDSE value 1.55. A finite positive optimum thus arises when the growing conjugate-quadrature contribution balances the initially dominant amplitude contribution. Unlike the leading-order normalized variance, the position of this optimum depends on the absolute vacuum-field amplitude and hence on the mode volume, since $\kappa \propto V^{-1}_{\mathrm{eff}}$ at fixed mean field and mode frequency.

Both the leading scaling in Eq. (23) and the conjugate-quadrature turnover are reproduced by a three-dimensional strong-field approximation calculation and benchmarked against the stochastic TDSE ensemble. This agreement supports the robustness of the underlying fluctuation mechanisms across the binding potentials, numerical methods, and continuum dimensionalities examined here. The benchmark results, coefficients, residual finite-pulse correction to the depth of the minimum, and assessment of the truncation's validity are provided in the Supplemental Material [34].

IV. DISCUSSION

The witness established above concerns the driving field alone: Our result does not imply that the emitted harmonic field is itself squeezed or otherwise nonclassical. The cutoff-variance criterion is not restricted to Gaussian squeezed states. More generally, the cutoff fluctuations probe the field noise along the quadrature selected by the strong-field response. Consequently, any Gaussian or non-Gaussian state with subvacuum fluctuations in that quadrature can, in principle, produce a sub-SQL cutoff variance. The criterion is nevertheless sufficient rather than necessary for optical nonclassicality. Nonclassical states without quadrature squeezing, including nonvacuum Fock states and certain nonclassical Fock-diagonal mixtures, need not produce a sub-SQL signal. Similarly, noise suppression in a quadrature to which the cutoff is insensitive will not be detected. The exponential scaling reported here is therefore specific to the SCS considered, whereas the underlying nonclassicality criterion is more general.

Several theoretical limitations should also be emphasized. The present analysis assumes a prescribed, undepleted

single-mode Gaussian driver. Propagation through a macroscopic medium, spatially varying nanophotonic near fields, mode mixing, and phase matching may further modify both the absolute cutoff variance and its normalized response. Multimode effects and optical loss are discussed in the Supplemental Material [34].

Experimental implementation requires an intense, phase-stable SCS, rather than the bright squeezed vacuum employed in several recent strong-field experiments. Emerging methods for ultrafast quantum-light generation and control indicate a possible route toward such states at midinfrared wavelengths [47]. In principle, gold bow-tie nanoantenna geometries explored for plasmon-enhanced HHG in noble gases [26,48] could provide a platform for experimental implementation, with the effective mode volume tailored through nanofabrication [49]. Optical loss in the driving field is another experimental consideration. For a pure-loss channel with transmissivity η, the normalized cutoff variance becomes $\mathcal{R}_\eta(r) \simeq \eta e^{-2r} + (1-\eta)$, using a coherent-state reference at the same transmitted mean field. Pure loss weakens the sub-SQL suppression but cannot generate a sub-SQL signal from a classical input within this regime (see the Supplemental Material [34]). The measurement itself requires only shot-resolved HHG spectra and avoids direct quadrature reconstruction by homodyne detection. Its main experimental challenge is separating quantum fluctuations from technical contributions such as mean-field drift and carrier-envelope-phase noise. Interleaved acquisition of coherent-state reference spectra under otherwise identical conditions would provide an operational SQL calibration and facilitate common-mode noise rejection, while the residual technical-noise variance would need to be independently characterized or bounded.

Beyond HHG, other nonlinear processes, such as high-order above-threshold ionization (HATI), are also sensitive to the quantum statistics of the driving field [23–25]. The ponderomotive scaling of HATI and direct-photoelectron cutoff energies motivates exploring whether their shot-to-shot fluctuations could provide similar nonclassicality witnesses. Changes in the mean cutoff or spectral shape alone, however, do not establish sub-SQL cutoff fluctuations. Extending the present criterion would require a dedicated analysis of the quadrature-dependent response, including ionization and, for HATI, rescattering, together with a consistently defined cutoff observable and comparison with a coherent-state reference.

V. CONCLUSION

We have shown that amplitude-squeezed driving can reduce the shot-to-shot variance of the HHG cutoff below the coherent-state SQL. Normalizing this variance to that of a coherent-state driver under otherwise identical conditions gives the ratio $\mathcal{R}$. Within the linear-response regime, $\mathcal{R} < 1$ certifies subvacuum noise in the driving-field quadrature sampled by the strong-field response and thus provides a sufficient, though not necessary, witness of optical nonclassicality.

Our central result is the scaling $\mathcal{R}(r) \simeq e^{-2r}$ in the moderate-squeezing regime. To leading order, this ratio is independent of the absolute vacuum-field amplitude and the effective mode volume. Normalization therefore removes the common $\mathcal{E}_{\mathrm{vac}}^2$ scale, allowing the squeezing-induced variance suppression to be identified without requiring an independent determination of the effective nanoscale mode volume within this approximation. At stronger squeezing, higher-order contributions from the antisqueezed quadrature compete with this suppression. The antisqueezed quadrature's quadratic coupling to the field modulus predicts a finite optimal squeezing strength near $r_{\mathrm{opt}} \approx 1.65$ for the parameters considered here.

These results show how quantum fluctuations of a driving field can be probed through an experimentally accessible strong-field observable without direct homodyne reconstruction or photon-number-resolved measurements of the driving mode. Although demonstrated here for SCS, the linear-response criterion applies more generally to states with subvacuum fluctuations in the sampled quadrature. Related processes, such as nonsequential double ionization and strong-field photoelectron interferometry, may offer further opportunities to probe field-quadrature fluctuations through their nonlinear response. Establishing analogous nonclassicality witnesses in these settings will require identifying the sampled quadratures and determining how their fluctuations enter the measured observable.

ACKNOWLEDGMENT

This work was supported by the Australian Research Council through the Discovery Project program (Grant No. DP230101253).

T.K. conceived the theoretical framework, developed and implemented the stochastic TDSE simulation code, performed all numerical calculations, and wrote the manuscript. R.T.S. and I.L. supervised the project, provided critical guidance on the theoretical interpretation and manuscript preparation, and reviewed and revised the manuscript. All authors discussed the results and approved the final version.

DATA AVAILABILITY

The data that support the findings of this study are available from the corresponding author upon reasonable request.

[1] P. B. Corkum, Plasma perspective on strong field multiphoton ionization, Phys. Rev. Lett. **71**, 1994 (1993).

[2] M. Lewenstein, Ph. Balcou, M. Yu. Ivanov, A. L'Huillier, and P. B. Corkum, Theory of high-harmonic generation by low-frequency laser fields, Phys. Rev. A **49**, 2117 (1994).

[3] M. Hentschel, R. Kienberger, C. Spielmann, G. A. Reider, N. Milosevic, T. Brabec, P. Corkum, U. Heinzmann, M. Drescher, and F. Krausz, Attosecond metrology, Nature (London) **414**, 509 (2001).

[4] P.-M. Paul, E. S. Toma, P. Breger, G. Mullot, F. Augé, P. Balcou, H. G. Muller, and P. Agostini, Observation of a train of attosecond pulses from high harmonic generation, Science **292**, 1689 (2001).

[5] B. Walker, B. Sheehy, L. F. DiMauro, P. Agostini, K. J. Schafer, and K. C. Kulander, Precision measurement of strong

field double ionization of helium, Phys. Rev. Lett. **73**, 1227 (1994).

[6] D. N. Fittinghoff, P. R. Bolton, B. Chang, and K. C. Kulander, Observation of nonsequential double ionization of helium with optical tunneling, Phys. Rev. Lett. **69**, 2642 (1992).

[7] T. Sh. Iskhakov, A. M. Pérez, K. Y. Spasibko, M. V. Chekhova, and G. Leuchs, Superbunched bright squeezed vacuum state, Opt. Lett. **37**, 1919 (2012).

[8] M.V. Chekhova, G. Leuchs, and M. Żukowski, Bright squeezed vacuum: Entanglement of macroscopic light beams, Opt. Commun. **337**, 27 (2015).

[9] A. M. Pérez, P. R. Sharapova, S. S. Straupe, F. M. Miatto, O. V. Tikhonova, G. Leuchs, and M. V. Chekhova, Projective filtering of the fundamental eigenmode from spatially multimode radiation, Phys. Rev. A **92**, 053861 (2015).

[10] A. Rasputnyi, Z. Chen, M. Birk, O. Cohen, I. Kaminer, M. Krüger, D. Seletskiy, M. Chekhova, and F. Tani, High-harmonic generation by a bright squeezed vacuum, Nat. Phys. **20**, 1960 (2024).

[11] S. Lemieux, S. A. Jalil, D. N. Purschke, N. Boroumand, T. J. Hammond, D. Villeneuve, A. Naumov, T. Brabec, and G. Vampa, Photon bunching in high-harmonic emission controlled by quantum light, Nat. Photon. **19**, 767 (2025).

[12] J. Heimerl, A. Rasputnyi, J. Pölloth, S. Meier, M. Chekhova, and P. Hommelhoff, Quantum light drives electrons strongly at metal needle tips, Nat. Phys. **21**, 1899 (2025).

[13] Z. Jiang, S. Pan, J. Chen, M. Zhu, C. Zhao, Y. Wang, R. Zhang, J. Lu, L. Han, S. Xiong, D. Wu, W. Li, S. Jiang, H. Ni, and J. Wu, Nonlinear atomic tunnelling boosted by bright squeezed vacuum, Nature (London) **654**, 356 (2026).

[14] M. E. Tzur, M. Birk, A. Gorlach, M. Krüger, I. Kaminer, and O. Cohen, Photon-statistics force in ultrafast electron dynamics, Nat. Photon. **17**, 501 (2023).

[15] A. Gorlach, M. E. Tzur, M. Birk, M. Krüger, N. Rivera, O. Cohen, and I. Kaminer, High-harmonic generation driven by quantum light, Nat. Phys. **19**, 1689 (2023).

[16] U. Bhattacharya, T. Lamprou, A. S. Maxwell, A. Ordóñez, E. Pisanty, J. Rivera-Dean, P. Stammer, M. F. Ciappina, M. Lewenstein, and P. Tzallas, Strong-laser-field physics, nonclassical light states and quantum information science, Rep. Prog. Phys. **86**, 094401 (2023).

[17] J. Rivera-Dean, P. Stammer, M. F. Ciappina, and M. Lewenstein, Structured squeezed light allows for high-harmonic generation in classical forbidden geometries, Phys. Rev. Lett. **135**, 013801 (2025).

[18] F. Wang, C. Yang, X. Cui, L. He, T. Ou, R.-B. Jin, Q. Liao, P. Lan, and P. Lu, Quantum path control in high-order harmonic generation via squeezed lights, Phys. Rev. A **112**, 043119 (2025).

[19] S.-J. Wang, X.-Y. Lai, and X.-J. Liu, Attosecond pulse synthesis from high-order harmonic generation in intense squeezed light, Phys. Rev. A **112**, L011102 (2025).

[20] L. Petrovic, P. Stammer, M. Lewenstein, and J. Rivera-Dean, Generation of circularly polarized high-order harmonics from single-color quantum light, Phys. Rev. A **114**, 013127 (2026).

[21] M. E. Tzur, M. Birk, A. Gorlach, I. Kaminer, M. Krüger, and O. Cohen, Generation of squeezed high-order harmonics, Phys. Rev. Res. **6**, 033079 (2024).

[22] J. Li, Z. Lyu, H. Liu, and Y. Liu, Quantum-optical signatures of solid-state high-harmonic generation driven by squeezed coherent states, Phys. Rev. A **112**, 033507 (2025).

[23] D. Habibović and D. B. Milošević, Intensity-dependent enhancements in strong-field ionization by quantum light, Phys. Rev. A **112**, L051103 (2025).

[24] S.-J. Wang and X.-Y. Lai, High-order above-threshold ionization of an atom in intense quantum light, Phys. Rev. A **108**, 063101 (2023).

[25] D. Habibović and D. B. Milošević, High-order above-threshold ionization by squeezed coherent light, Phys. Rev. A **113**, 043124 (2026).

[26] S. Kim, J. Jin, Y.-J. Kim, I.-Y. Park, Y. Kim, and S.-W. Kim, High-harmonic generation by resonant plasmon field enhancement, Nature (London) **453**, 757 (2008).

[27] M. F. Ciappina, J. A. Pérez-Hernández, A. S. Landsman, W. A. Okell, S. Zherebtsov, B. Förg, J. Schötz, L. Seiffert, T. Fennel, T. Shaaran *et al.*, Attosecond physics at the nanoscale, Rep. Prog. Phys. **80**, 054401 (2017).

[28] M. Krüger, M. Schenk, and P. Hommelhoff, Attosecond control of electrons emitted from a nanoscale metal tip, Nature (London) **475**, 78 (2011).

[29] M. Sivis, M. Taucer, G. Vampa, K. Johnston, A. Staudte, A. Y. Naumov, D. M. Villeneuve, C. Ropers, and P. B. Corkum, Tailored semiconductors for high-harmonic optoelectronics, Science **357**, 303 (2017).

[30] G. Vampa, B. G. Ghamsari, S. S. Mousavi, T. J. Hammond, A. Olivieri, E. Lisicka-Skrek, A. Yu Naumov, D. M. Villeneuve, A. Staudte, P. Berini, and P. B. Corkum, Plasmon-enhanced high-harmonic generation from solid silicon, Nat. Phys. **13**, 659 (2017).

[31] K. E. Cahill and R. J. Glauber, Density operators and quasiprobability distributions, Phys. Rev. **177**, 1882 (1969).

[32] W. P. Schleich, *Quantum Optics in Phase Space* (Wiley-VCH, Berlin, 2001).

[33] C. Gardiner and P. Zoller, *Quantum Noise: A Handbook of Markovian and Non-Markovian Quantum Stochastic Methods with Applications to Quantum Optics*, 3rd ed. (Springer, Berlin, 2004).

[34] See Supplemental Material at https://link.aps.org/supplemental/10.1103/ffdj-mz2y for details of the numerical method and its validation, the vacuum-field estimate, the analytical derivations, the strong-field-approximation cross-check, and the multimode and optical-loss analyses of the classicality criterion, which includes Refs. [35–37].

[35] M. D. Feit, J. A. Fleck, Jr., and A. Steiger, Solution of the Schrödinger equation by a spectral method, J. Comput. Phys. **47**, 412 (1982).

[36] C. Weedbrook, S. Pirandola, R. García-Patrón, N. J. Cerf, T. C. Ralph, J. H. Shapiro, and S. Lloyd, Gaussian quantum information, Rev. Mod. Phys. **84**, 621 (2012).

[37] A. Huck, S. Smolka, P. Lodahl, A. S. Sørensen, A. Boltasseva, J. Janousek, and U. L. Andersen, Demonstration of quadrature-squeezed surface plasmons in a gold waveguide, Phys. Rev. Lett. **102**, 246802 (2009).

[38] Q. Su and J. H. Eberly, Model atom for multiphoton physics, Phys. Rev. A **44**, 5997 (1991).

[39] J. Javanainen, J. H. Eberly, and Q. Su, Numerical simulations of multiphoton ionization and above-threshold electron spectra, Phys. Rev. A **38**, 3430 (1988).

[40] L. V. Keldysh, Ionization in the field of a strong electromagnetic wave, Sov. Phys. JETP **20**, 1307 (1965).

[41] K. Burnett, V. C. Reed, J. Cooper, and P. L. Knight, Calculation of the background emitted during high-harmonic generation, Phys. Rev. A **45**, 3347 (1992).

[42] J. C. Baggesen and L. B. Madsen, On the dipole, velocity and acceleration forms in high-order harmonic generation from a single atom or molecule, J. Phys. B: At. Mol. Opt. Phys. **44**, 115601 (2011).

[43] M. V. Ammosov, N. B. Delone, and V. P. Kraĭnov, Tunnel ionization of complex atoms and of atomic ions in an alternating electromagnetic field, Sov. Phys. JETP **64**, 1191 (1986).

[44] R. L. Hudson, When is the Wigner quasi-probability density non-negative? Rep. Math. Phys. **6**, 249 (1974).

[45] R. J. Glauber, Coherent and incoherent states of the radiation field, Phys. Rev. **131**, 2766 (1963).

[46] E. C. G. Sudarshan, Equivalence of semiclassical and quantum mechanical descriptions of statistical light beams, Phys. Rev. Lett. **10**, 277 (1963).

[47] M. Sennary, J. Rivera-Dean, M. ElKabbash, V. Pervak, M. Lewenstein, and M. T. Hassan, Attosecond quantum uncertainty dynamics and ultrafast squeezed light for quantum communication, Light Sci. Appl. **14**, 350 (2025).

[48] A. Husakou, S.-J. Im, and J. Herrmann, Theory of plasmon-enhanced high-order harmonic generation in the vicinity of metal nanostructures in noble gases, Phys. Rev. A **83**, 043839 (2011).

[49] D. K. Oh, Y. Kim, J. Kim, I. Kim, and J. Rho, Guided domino lithography for uniform fabrication of single-digit-nanometer scale plasmonic nanoantenna, Nanophotonics **12**, 1435 (2023).